Quantification of Volcano Deformation caused by Volatile Accumulation and Release

A. Spang [1], **M. Burton** [2], **B. J. P. Kaus** [1,4], **F. Sigmundsson** [3]

[1]Johannes Gutenberg University, Institute of Geosciences, Johann-Joachim-Becher-Weg 21, 55128 Mainz,

Germany

[2]School of Earth and Environmental Sciences, University of Manchester, Manchester M13 9PL, UK

[3]Nordic Volcanological Center, Institute of Earth Sciences, University of Iceland, Askja, Sturlugata 7,

Reykjavik IS-101, Iceland

[4]TeMaS, Terrestrial Magmatic Systems Research Center, temas.uni-mainz.de

Key Points:

- Exsolving volatiles accumulate at the roof of a magma storage zone and contribute to surface deformation through buoyancy forces
- 3D numerical models show that surface deformation is a function of the volatiles' volume, density and depth as well as crustal rigidity
- Volatile release during eruption can cause syn-eruptive subsidence of a few cm, which is 20% of the observed signal at Calbuco in 2015

Corresponding author: Arne Spang, `arspang@uni-mainz.de`

Abstract

Crustal-stored magma reservoirs contain exsolved volatiles which accumulate in the reservoir roof, exerting a buoyancy force on the crust. This produces surface uplift and sudden loss of volatiles through eruption results in syn-eruptive subsidence. Here, we present three-dimensional, visco-elasto-plastic, numerical modeling results which quantify the ground deformation arising from the growth and release of a volatile reservoir. Deformation is mostly independent of crustal thermal distribution and volatile reservoir shape, but is a function of volatile volume, density and depth and crustal rigidity. We present a scaling law for the volatiles' contribution to syn-eruptive subsidence and show this contributes ∼20% of the observed subsidence associated with the 2015 Calbuco eruption. Our results highlight the key role that volatile-driven buoyancy can have in volcano deformation, show a new link between syn-eruptive degassing and deflation, and highlight that shallow volatile accumulation and release may have a significant impact on ground deformation of volcanoes.

Plain Language Summary

Magma contains a lot of gases which separate from it when it approaches the surface. These gases can collect right above the magma storage region a few kilometers below the surface. They have a much lower density than the rocks surrounding them and push upwards like a balloon filled with air that is pressed under water. In this study, we use computer models to understand how much a volcano would grow from the push of the gases below and how much it would shrink when the gases escape because of an eruption. We find that the gases can cause the volcano to grow and shrink up to a few centimeters during accumulation and release, respectively. The amount of surface movement depends on the volume, density and depth of the gas reservoir as well as on the toughness of the rocks above it. We derive a simple equation which allows us to compute the surface movement using the aforementioned parameters. With this equation and estimates about the amount of accumulated gas at the 2015 Calbuco eruption, we can assume that about 20% of the observed surface movement was caused by the release of the magmatic gases.

Index Terms

8145 Physics of magma and magma bodies

48   1211 Non-tectonic deformation

49   0545 Modeling

50   8430 Volcanic gases

51   1036 Magma chamber processes

Keywords

3D modeling, Buoyancy, Volcanic uplift, Scaling analysis, Magmatic gases, Calbuco

1 Introduction

Volcano deformation is most frequently interpreted in terms of models of surface deformation due to processes in magma bodies of various geometries. The most widely applied model is that of a point source of pressure embedded within a uniform elastic halfspace (Mogi, 1958), but a range of more advanced models and approaches exist (e.g. Fialko et al., 2001a; Hickey et al., 2016). As liquid magma flows in/out of the these deformation sources, they expand/contract. Most often, such magma flow is considered to cause uniform pressure change on the boundary of the magma body, and the density difference between magma and host rock is not considered specifically. It has, however, been demonstrated in a number of studies that magma buoyancy can cause significant stresses in volcano roots and contribute to failure of magma bodies (e.g. Sigmundsson et al., 2020). A particular phenomena not considered by traditional volcano deformation models is the effect of accumulated exsolved volatiles in volcano roots and their release during eruptions.

During major explosive eruptions an excess of gas may be observed, beyond that which can be explained by a petrological calculation of the original dissolved volatile amounts and the volume of erupted lavas. Excess gas was observed in the 1991 eruption of Pinatubo, Philippines and an analysis from Wallace and Gerlach (1994) showed that this could be explained by a pre-existing gas/volatile phase representing 0.7 to 1.3 wt% of the erupted magma. Volatile accumulation was proposed to occur in the roof zone of the system. On 22 April 2015, the Chilean volcano Calbuco produced a sub-Plinian eruption (Castruccio et al., 2016; Romero et al., 2016; Arzilli et al., 2019) with two explosive phases. The first was found to be powered by an excess gas phase with three times the amount of SO_2 estimated to be produced by the erupted mass (Pardini et al., 2018). In highly silicic systems, the volume of erupted products may be only a fraction of the magma reservoir vol-

ume, as eruptible magma is extracted from a large crystal mush (e.g. Bachmann & Bergantz, 2004). This creates the possibility that a voluminous volatile body is created within magmatic systems prior to eruption, ponding in the roof zone, producing both observed excess gas and a buoyancy force on the crust, arising from the volatiles lower density ($\sim$ 500 $\mathrm{kg\,m^{-3}}$) compared with melt and crust. At a depth of 8 km and pressure of 200 MPa, the solubility of CO_2 in a basalt is $\sim$ 700 ppm (Newman & Lowenstern, 2002), while the initial CO_2 contents may be 1 wt% (10,000 ppm) or greater (Blundy et al., 2010). So a significant free volatile phase can be expected in magma reservoirs if the volatiles exsolve but cannot escape to the surface. The purpose of this study is to examine the impact of the sudden release of a large volume of exsolved volatiles and the associated loss of buoyancy to estimate the significance of this process for volcano deformation modeling.

To do that, we utilize the three-dimensional (3D) thermomechanical finite differences code LaMEM (Kaus et al., 2016) to model the stresses and deformation that a sudden change in the density field induces in the overlying crust and at the surface. LaMEM solves the density dependent Stokes equations for (nearly) incompressible visco-elasto-plastic fluid flow and runs on massively parallel clusters, allowing us to use high resolutions, even in 3D. The code has already been applied to magmatic systems before (e.g. Reuber et al., 2018; Piccolo et al., 2020; Spang et al., 2021).

2 Methods

Section 2.1 introduces the software used for modeling as well as the physics and governing equations. Section 2.2 presents the model setup and the parameters used. Details on model resolution, time stepping and resolution tests are presented in supplementary text S1. Section 2.3 describes the key parameters that we identified and our approach to deriving a scaling law for the surface deformation due to volatile release. In section 2.4, we introduce our area of application, the Chilean volcano Calbuco.

2.1 Thermomechanical Code

The 3D thermomechanical finite differences code LaMEM (Kaus et al., 2016) was used to calculate deformation due to magmatic sources hosted in a finite-size model domain. The code solves for the conservation of momentum, mass and energy (eq. 1-3),

using a staggered grid in combination with a marker-in-cell approach (Harlow & Welch, 1965).

$$\frac{\partial \tau_{ij}}{\partial x_j} - \frac{\partial p}{\partial x_i} + \rho g_i = 0 \tag{1}$$

$$\frac{\partial v_i}{\partial x_i} = 0 \tag{2}$$

$$\rho C_p \frac{DT}{Dt} = \frac{\partial}{\partial x_i}\left(k \frac{\partial T}{\partial x_i}\right) + H \tag{3}$$

τ_{ij} is the Cauchy stress deviator, $x_i (i = 1, 2, 3)$ denotes the Cartesian coordinates, p is pressure (positive in compression), ρ density, g_i gravitational acceleration, v_i the velocity vector, C_p the specific heat capacity, T the temperature, k the thermal conductivity, H the volumetric heat source and D/Dt is the material time derivative.

Free slip conditions are applied to the boundaries of the model domain, allowing movement parallel to the domain edges while setting perpendicular velocities to 0. At the top of the setup, we include 1 km of sticky air above the stabilized free surface (Duretz et al., 2011; Kaus et al., 2010). The rocks are characterized by a temperature- and strain rate-dependent visco-elasto-plastic rheology where the strain rate is the sum of the elastic, viscous and plastic components:

$$\dot{\epsilon}_{ij} = \dot{\epsilon}_{ij}^{el} + \dot{\epsilon}_{ij}^{vi} + \dot{\epsilon}_{ij}^{pl} \tag{4}$$

$\dot{\epsilon}_{ij}$ denotes the total deviatoric strain rate tensor, while $\dot{\epsilon}_{ij}^{el}$, $\dot{\epsilon}_{ij}^{vi}$ and $\dot{\epsilon}_{ij}^{pl}$ represent the elastic, viscous and plastic strain rate components. A detailed discussion of this equation and all of its components is given by Kaus et al. (2016), but here we will focus on the material parameters which impact the three components.

The elastic component $\dot{\epsilon}_{ij}^{el}$ is inverse proportional to the shear modulus G:

$$\dot{\epsilon}_{ij}^{el} = \frac{1}{2G} \frac{D\tau_{ij}}{Dt}, \tag{5}$$

where $D\tau_{ij}/Dt$ corresponds to the objective derivative of the stress tensor.

The viscous strain rate component $\dot{\epsilon}_{ij}^{vi}$ is governed by the viscosity η, which follows the temperature- and strain rate-dependent powerlaw relationship of dislocation creep:

$$\eta = \frac{1}{2}(B_n)^{-\frac{1}{n}}(\dot{\epsilon}_{II})^{\frac{1}{n}-1}\exp\left(\frac{E_n}{nRT}\right), \tag{6}$$

where B_n is the creep constant, $\dot{\epsilon}_{II}$ the square root of the second invariant of the strain rate ($\dot{\epsilon}_{II} = (\frac{1}{2}\dot{\epsilon}_{ij}\dot{\epsilon}_{ij})^{1/2}$), E_n the activation energy, n the powerlaw exponent, R the universal gas constant and T the temperature.

The plastic component is characterized by the Drucker-Prager failure criterion (Drucker & Prager, 1952) which is a good approximation of Byerlee's law (Byerlee, 1978):

$$\tau_{II} \leq \sin(\phi)p + \cos(\phi)c_0 \tag{7}$$

τ_{II} is the square root of the second invariant of the stress tensor ($\tau_{II} = (\frac{1}{2}\tau_{ij}\tau_{ij})^{1/2}$), ϕ is the friction angle, p the pressure and c_0 the cohesion. Equation 7 describes how much stress can be accommodated with visco-elastic deformation.

As buoyancy is the driving force in our model, we need densities to be independent of temperature (i.e. no thermal expansion) and pressure (i.e. incompressible). For the volatile reservoir, we use the ideal gas law to estimate density (see supplementary text S2).

2.2 Model Setup and Parameter Selection

Obtaining a quantitative understanding of ground deformation requires the use of 3D models, but as they are computationally expensive, we do initial testing in 2D which allows an efficient evaluation of the respective importance of various model parameters.

Our reference model (Figure 1a) uses a homogeneous crust, hosting a spherical, low-viscosity, non-buoyant magma reservoir with a radius of 1 km. As exsolved volatiles are expected to accumulate in the roof of the magmatic system, we approximate the volatile reservoir as a sphere (r = 250 m) of low density, viscosity and rigidity on top of the magma body. We use a non-buoyant magma body to focus on the volatiles' contribution to surface deformation. It still provides heat to the surrounding host rock and mechanically decouples the volatile reservoir from the underlying crust.

To approximate the release of the exsolved volatiles from the system during eruption, they are instantaneously replaced by non-buoyant magma after 20 years (the time

154 of eruption in the model). This is accomplished by copying the material properties (den-

155 sity, viscosity and shear modulus) of the magma onto the volatile particles. The change

156 in density induces a change in crustal stresses (see equation 1, supplementary Figure S1).

157 In reality, an eruption does not only remove the buoyancy forces of the volatile reser-

158 voir but also the volatiles themselves as well as part of the magma. As magma injection

159 is a commonly suggested trigger for eruptions (Canon-Tapia, 2014), the erupted volume

160 may be replaced by intruding magma from a deep source. If this is not or only partly

161 the case, the loss of volume leads to a depressurization of the remaining magma reser-

162 voir. This likely triggers a combination of three processes. (i) The remaining magma ex-

163 solves more volatiles due to the drop in confining pressure which expand upon exsolu-

164 tion. (ii) The magma itself expands due to depressurization. (iii) The overburden sub-

165 sides and contracts to close the space left behind. All of these processes influence sur-

166 face deformation alongside the loss of buoyancy, but as the contribution of each of the

167 three aforementioned processes and magma injection is not understood, we focus on the

168 change in buoyancy forces. This way, we can constrain the magnitude of this individ-

169 ual contributor to syn-eruptive subsidence and estimate whether it is significant.

170 Supplementary table S1 shows the parameters we use for the different model ma-

171 terials. The rheology of the crust follows the powerlaw relationship of dislocation creep

172 of wet quartzite (Ranalli, 1995) while magma and volatile reservoir are linear visco-elasto-

173 plastic. We use a shear modulus of 2 GPa, in line with upscaled values from laboratory

174 experiments on volcanic rocks (Heap et al., 2020). Cohesion and friction angle of intact

175 rocks are typically estimated in the range of a few MPa and 30° respectively (Hoek &

176 Brown, 1997), so we use 5 MPa and 20° for the presumably pre-damaged crust of a mag-

177 matic system. The thermal conductivity is 3 $W\,(m\,K)^{-1}$ and the heat capacity 1000 $J\,(mol\,K)^{-1}$

178 for all materials. We employ a background thermal gradient of 30 $K\,km^{-1}$ and set the

179 initial temperature of volatiles and magma to 800 °C. Before we start the mechanical

180 model (t = 0), we allow for 50 kyr of thermal diffusion to account for the heated crust

181 around a magma body which we keep at a constant temperature during this heating phase.

2.3 Scaling Law for Deflation

183 Through initial testing, we identified four key parameters that influence the ground

184 deformation (Figure 1b). The radius of the volatile reservoir (r_{vol}), the depth of the volatile

reservoir (d_{vol}), the density contrast between volatiles and crust ($\Delta\rho$) and the shear modulus of the crust (G_{crust}). In both 2D and 3D, we run a set of systematic parameter combinations to derive a scaling law for the deflation at the surface due to the volatile removal. For each parameter, we test 5 (9 for d_{vol}) different values while keeping the others constant.

2.4 Calbuco

The Chilean stratovolcano Calbuco erupted on April 22, 2015 and interferometric analysis of synthetic aperture radar images (InSAR analysis) from the Sentinel-1 satellites revealed a co-eruptive subsidence of about 12 cm (Nikkhoo et al., 2016; Delgado et al., 2017). Using different analytical solutions, Nikkhoo et al. (2016) and Delgado et al. (2017) reproduce the surface deformation with deflating sources at a depth of around 8 km. Petrological estimates for the location of the magma storage zone range from 5.5 to 12 km depth (Morgado et al., 2019; Arzilli et al., 2019; Namur et al., 2020). Namur et al. (2020) also suggest that magma moved to shallower levels weeks or month prior to eruption.

Pardini et al. (2018) found that a pre-existing volatile phase must have been present to explain $1.5 \cdot 10^8$ kg of excess SO_2 produced by the Calbuco eruption. Assuming a typical arc-magma H_2O abundance of 3 wt% (100 times the SO_2 content (Pardini et al., 2018)), we expect that this pre-exsolved volatile phase would contain $1.5 \cdot 10^{10}$ kg of H_2O (Spilliaert et al., 2006). CO_2 is much less soluble than H_2O or SO_2 and therefore to calculate the pre-eruptive CO_2 content we conservatively estimate that the total mass of the magma reservoir was ten times (Annen et al., 2008) the erupted mass of $4.9 \cdot 10^{11}$ kg (Pardini et al., 2018). Assuming that 0.5–1.5 wt% of CO_2 (Blundy et al., 2010) was exsolved prior to eruption leads to pre-exsolved CO_2 masses of $2.5 \cdot 10^{10}$–$7.4 \cdot 10^{10}$ kg. We therefore estimate that the total pre-exsolved gas mass was $3.9 \cdot 10^{10}$–$8.8 \cdot 10^{10}$ kg. We consider two scenarios, with volatiles stored at 5.5 km and 8 km depth and use the ideal gas law and lithostatic pressure to estimate the density of the volatile reservoir (see supplementary text S2).
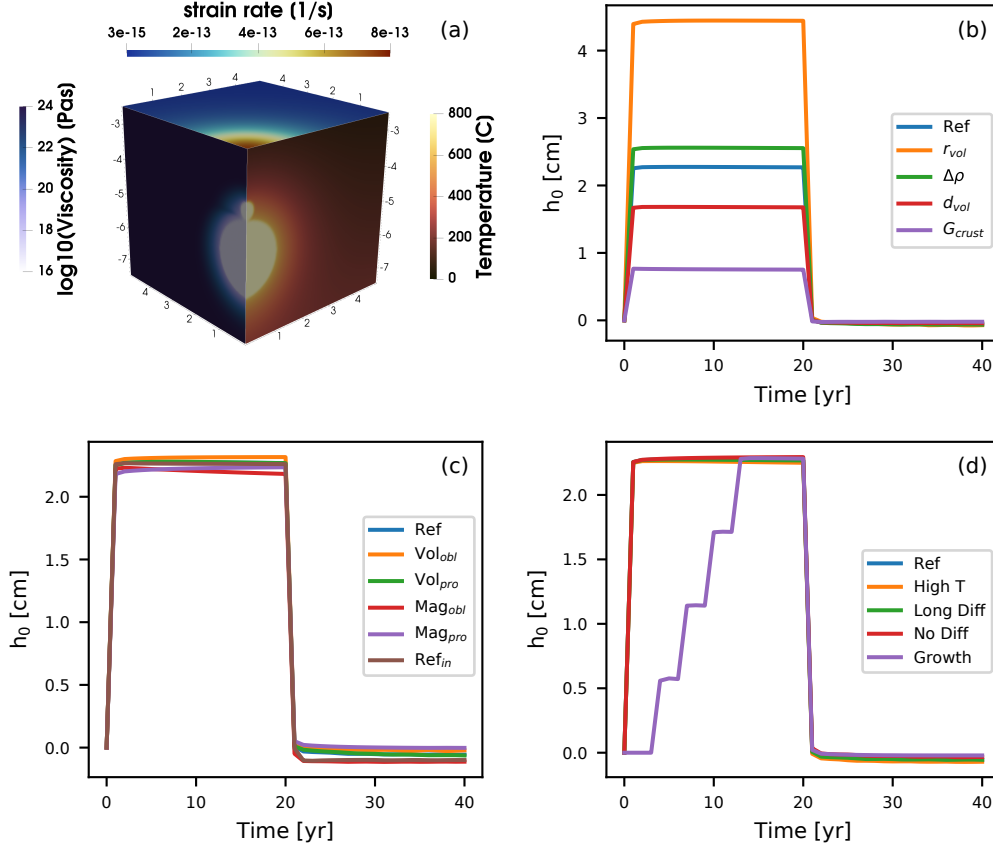
Figure 1. (a) Zoomed in part of 3D model setup showing the viscosity on the left panel, temperature on the right panel, and strain rate on the top panel before the release of the volatiles. The 2D setup is a slice along the boundary of the 3D model. 2D and 3D model both extend 50 km in lateral and 15 km in vertical direction but those parts of the figure were cut to enlarge the relevant features. Axes are in km. (b-d) Surface level directly above the sources calculated in 3D models. (b) Effect of perturbing one crucial material parameter compared to the reference model. (c) Effect of changing the shape of the magma and volatile reservoir in comparison to reference model. Subscript $_{obl}$ means oblate, subscript $_{pro}$ means prolate. The volume was preserved in all cases. Ref$_{in}$ corresponds to a model where the volatile reservoir is placed inside the magma body. (d) Effect of changing the temperature structure in the crust through higher reservoir temperature or longer/no initial diffusion time. See section 3.2 for details. 'Growth' corresponds to a model where the volatile reservoir incrementally increases in size.

3 Results

Section 3.1 describes the general behavior of the model and discusses dependencies on time stepping and size of the model domain. In section 3.2, we discuss the effects of changing the geometry of the magma body and volatile reservoir as well as the thermal structure of the crust. Section 3.3 describes the derivation of the scaling law in 3D. The 2D is scaling law is discussed in supplementary text S3 and the differences between 2D and 3D in supplementary text S4. In section 3.4 we apply the scaling law derived in section 3.3 to the case of the 2015 Calbuco eruption.

3.1 General Behavior

At the start of each simulation, the surface above the buoyant volatile reservoir undergoes immediate uplift, and quickly (within 2 time steps) reaches a steady state. Upon, replacing the volatiles with non-buoyant magma (i.e. an eruption), the surface quickly (within 2 time steps) returns to the original level. Independently of the time step we employ (0.1 - 10 years), the surface reaches the same level after 2 steps with the first step being very close to it already (Figures S2c and S3d). We observe the same behavior after removing the volatile reservoir. We therefore conclude that the surface response is immediate and has no time dependence. The small adjustment, necessary in the second time step, is inferred to be of numerical origin. To minimize computational cost and enable us to observe any potential time dependencies, we use a time step of 1 year for all our models. In reality, the uplift or inflation phase may take place over a long time as the volatile reservoir grows gradually, but will reach the same magnitude as in our models. Volcano deflation, however happens on timescales of eruptions as all volatiles are expected to reach the surface, once a pathway has been established.

Supplementary Figures S2d and S3c show that the surface displacement depends on the width of the model domain. The displacement increases with increasing model width but at 50 km width, the effect levels off. We therefore ran all models with a width of 50 km.

We do not observe plastic failure in any of our models. Even after reducing cohesion (c_0) by an order of magnitude to 0.5 MPa and friction angle (ϕ) to 10° while increasing r_{vol} to 500 meters and G_{crust} to 10 GPa to maximize crustal stresses, stresses due

243   to changes in buoyancy never exceed a few MPa which is insufficient to exceed the Drucker-

244   Prager failure criterion.

3.2 Influence of Source Geometry and Thermal Structure

246   In Figure 1c, we show the results of testing different shapes for the magma and volatile

247   reservoirs. Both the oblate and prolate shapes have an aspect ratio of 2 while preserv-

248   ing the volume of the spherical version. None of the geometrical variations lead to a sig-

249   nificant difference in vertical displacement. Immersing the lower half or the entire volatile

250   reservoir in the top of the magma body does not have significant effects either (Figure

251   1c).

252   Figure 1d shows the effect of changing the thermal structure of the crust. In the

253   'No Diff' example, we omit the 50 ka of thermal diffusion and start with a crust that only

254   has the background temperature gradient while in the 'Long Diff' example, we double

255   the temperature diffusion time from 50 to 100 ka. For the 'High T' example, we set the

256   magma and volatile temperature to $1000\,^{\circ}\mathrm{C}$ instead of $800\,^{\circ}\mathrm{C}$. The surface response is

257   almost identical with the reference model for all cases.

3.3 3D Scaling law

259   Figure 1b shows the effect of varying four material parameters that have a consid-

260   erable effect on the surface response. The radius and depth of the volatile reservoir (d),

261   the density contrast between volatiles and crust ($\Delta\rho$) and the shear modulus of the crust

262   (G). We performed a systematic parameter variation, testing 5 different values for each

263   parameter (9 for d_{vol}) while keeping the other parameters constant. Supplementary Fig-

264   ure S6 shows the results for individual parameters. From this, we are able to derive the

265   following scaling relationship:

$$\Delta h_0 = A \frac{r^3 \, \Delta\rho \, g}{d^{3/2} \, G} \tag{8}$$

266   where Δh_0 is the vertical displacement at the surface above the source, g is the grav-

267   itational acceleration and A is a pre-factor of $12\,\pi$ with units of $\mathrm{m}^{0.5}$ to satisfy the equa-

268   tion. The scaling law is similar to the one derived for the 2D case with the only excep-
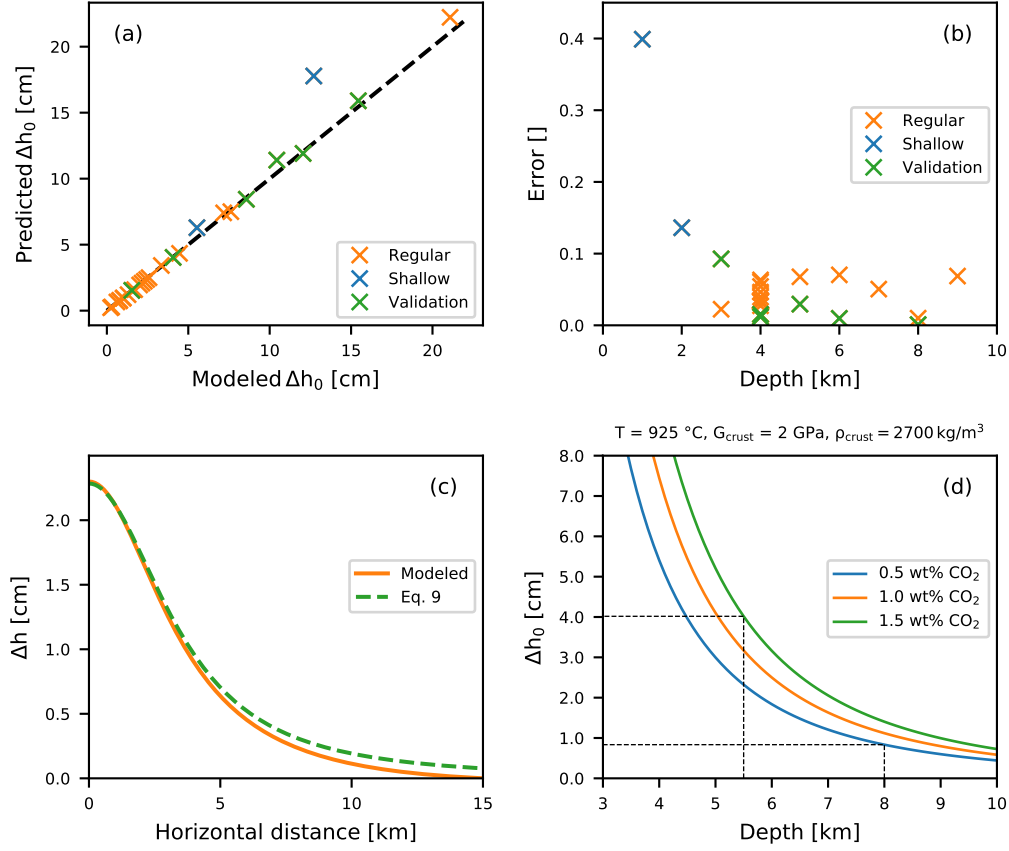
–11–

Figure 2. (a) Comparison between modeled subsidence and subsidence predicted by equation 8. Black dashed line shows 1:1 correlation. Orange crosses show models that were used to derive equation 8 and green crosses show models used to validate the scaling law. Blue crosses show models with a shallow ($<= 2\,\text{km}$) volatile reservoir that were excluded. (b) Error between the modeled subsidence and the predicted subsidence as a function of depth. (c) Subsidence along a radial profile for the reference case in orange in comparison to the prediction made by equation 9. Offset at the edge is due to the boundary conditions of the model as the uplift in the center needs to be balanced by subsidence along the edges. (d) Coupling between the ideal gas law and equation 8 to show the full dependence of maximum subsidence Δh_0 on reservoir depth d. Solid lines denote different volatile mass estimates as discussed in section 2.4. Dashed black lines show how we determine the minimum and maximum of subsidence in section 3.4.

269   tion being the exponents of r and d (see equation S4). Fits for the individual parame-

270   ters are shown in Figure S6.

271   Figure 2a shows how equation 8 predicts the results of the 3D models and Figure

272   2b shows the error which is generally smaller than 10%. Green crosses in Figures 2a and

273   2b show models where we changed multiple parameters to validate equation 8. Subsi-

274   dence in models with a shallow ($d <= 2\,km$) volatile reservoir are overestimated. An-

275   alytical solutions for the gravity anomaly of buried cylinders or spheres have the same

276   issue of only being applicable when the depth of the body is much larger than its radius

277   (Turcotte & Schubert, 2002). The same is true for simple models relating the inflation

278   of magma bodies to surface deformation (e.g. Mogi, 1958; Yang et al., 1988).

279   Equation 8 only describes the vertical displacement directly above the center of the

280   volatile reservoir. Figure 2c shows a profile of the vertical change along the surface. Our

281   numerical models show that we can modify equation 8 to:

$$\Delta h(x) = A \frac{r^3 \, \Delta\rho \, g}{G} \frac{d}{(d^2 + x^2)^{5/4}} \tag{9}$$

282   where x is the horizontal distance from the center of the volatile reservoir projected to

283   the surface. Figure 2c shows that the modeled surface displacement is fit well by equa-

284   tion 9. In this form, our scaling law is very similar to the analytical solution of ground

285   deformation due to a point source of pressure within an elastic halfspace, the "Mogi model"

286   (Mogi, 1958). The most notable difference being the exponent of 5/4 instead of 3/2, which

287   stems from the depth dependence of $\frac{1}{d^{3/2}}$ (see equation 8 and supplementary Figure S6c)

288   while the "Mogi model" has a depth dependence of $\frac{1}{d^2}$.

3.4 Calbuco

290   For Calbuco, we use equation 8 with $\rho_{\mathrm{crust}} = 2700\,\mathrm{kg\,m^{-3}}$ and $\mathrm{G_{crust}} = 2\,\mathrm{GPa}$ to

291   predict a maximum surface subsidence of 4 cm due to the loss of buoyancy from $8.8 \cdot 10^{10}$

292   kg of exsolved volatiles for the case of storage at 5.5 km depth. For the 8 km depth sce-

293   nario, and a lower limit estimate of the erupted gas mass ($3.9 \cdot 10^{10}$ kg), we predict 1 cm.

294   Equations 8 and 9 imply that the surface displacement depends on the reservoir depth

295   to the power of 1.5. In reality, r and $\Delta\rho$ are also functions of the pressure in the volatile

reservoir and thereby of the depth. Figure 2d illustrates this nonlinear dependence and shows how we arrive at our minimum and maximum estimates.

4 Discussion

4.1 Rheology

Given that, even for rocks with considerably lowered plastic strength, the stresses caused by the changes in buoyancy are not sufficient to exceed the failure criterion, plasticity is not a relevant factor in our models. Figure 1d also suggests that on the timescales of an eruption, viscous components have no impact on the deformation, even with the weakening caused by heating of the crust. The process of surface subsidence caused by the loss of a buoyant volatile reservoir due to eruption can therefore be considered as quasi-elastic, and as a result it is possible to derive a scaling law for the problem.

4.2 Surface Subsidence due to Buoyancy Loss

Instantly (on the timescale of an eruption) removing the buoyancy forces, exerted by a volatile reservoir, from the top of an upper crustal magma body leads to an instantaneous subsidence. The magnitude of subsidence decays with radial distance from the reservoir center, but is significant in a radius of several kilometers (Figure 2c). The surface response is insensitive to the temperature structure (Figure 2d) of the crust which allows us to derive a scaling law for the expected subsidence (equations 8 and 9). As the shape of the volatile reservoir appears to play a minor role (Figure 1c), we suggest this alternative form of equation 9:

$$\Delta h(x) = \frac{9\,V\,\Delta\rho\,g}{G}\,\frac{d}{(d^2 + x^2)^{5/4}} \tag{10}$$

where V is the volume of the volatile reservoir. As other analytical solutions for the surface effects of buried bodies, the scaling law's accuracy decreases when the ratio between radius and depth of the body exceeds 0.1 (Figure 2b). The reduction to volume is in line with Archimedes' principle.

The inferred scaling law (equations 8, 9 and 10) has a similar structure to the Mogi model including a pre-factor, a cubic dependence on radius, an elastic property of the crust and a term describing the decay of the signal with distance. One difference is the

term of the driving force of deformation. In the Mogi model, it is either a pressure or a volume change, while in our scaling law, it is buoyancy. The other notable difference is the exponent of the depth dependence (2 for Mogi and 1.5 in our model). This could be caused by the different mechanisms that are at work. The pressure point source of the Mogi model applies a pressure to the surrounding crust in all directions, while in our case, buoyancy is expected to exert a cummulative upwards force in line with Archimedes' principle (e.g. Sigmundsson et al., 2020).

Another difference to common scaling laws for volcano deformation (e.g. Mogi, 1958; McTigue, 1987) is the lack of compressibility in our models because of its complex interplay with densities. As vertical displacement is usually multiplied by the term $(1 - \nu)$, our scaling law might provide a minimum estimate as a commonly used Poisson's ratio of $\nu = 0.25$ results in a larger factor than incompressibility ($\nu = 0.5$).

4.3 Calbuco

Applying our scaling law to the case of the 2015 Calbuco eruption, yields a subsidence of 1–4 cm (Figure 2d). With an incidence angle of 33° (Delgado et al., 2017), these vertical velocities can be projected into line-of-sight displacement (Fialko et al., 2001b) and represent 7% to 28% of the observed surface deformation. This is an indication that the majority of co-eruptive subsidence was caused by the volumetric loss of material (volatiles and magma) but a significant part of the signal may originate from the loss of buoyancy provided by a body of exsolved volatiles.

In fact, the best-fit sphere and spheroid models of Delgado et al. (2017) have a residual of about 3 cm in the center of subsidence. The mechanism described in our work provides an additional source of uplift, large enough to cover this misfit entirely.

4.4 Implications for Modeling Volcanic Deformation

The release of a buoyant body of exsolved volatiles from the top of an upper crustal magma reservoir can lead to significant (on the order of a few cm) syn-eruptive subsidence at the surface. This effect is likely smaller than the effect of volume change in volcanic roots during eruptions as magma moves to the surface. In the case of Calbuco, the contributions may have a ratio between 3:1 and 10:1 in favor of the volume loss. This ratio depends, however, on the quantity of pre-exsolved volatiles.

Adding equation 10 to existing models could be a simple way of achieving a better fit to the observed deformation while also providing an explanation for the excess gas that is detected for a number of eruptions.

As Figure 1 shows, the presence of a buoyant body of exsolved volatiles also causes surface uplift of the same magnitude as its removal causes subsidence. That means that inflation of a few centimeters over time, which is traditionally interpreted to be a sign of magma intrusion at depth, could also be caused by the formation of a body of exsolved volatiles at the top of the magma reservoir.

Furthermore, magma is usually buoyant at the depth where it intrudes. So even if the intruded magma does not form a significant volatile reservoir, it still exerts a buoyancy force on the crust that adds to the surface deformation caused by displacing host rock. Although the effect of magma buoyancy on surface deformation was not explicitly investigated here, it is likely that equation 10 also gives a good estimate of its effect and could be added to existing solutions for surface uplift.

5 Conclusions

We conducted a series of 3D visco-elasto-plastic models to investigate the surface deformation caused by the instantaneous removal of buoyancy forces, exerted by a reservoir of exsolved volatiles, from the top of a magma body, as would be the case during an eruption. Our results show that the removal causes subsidence at the surface which is mostly independent of the shape of the volatile and magma reservoirs as well as from the thermal state of the crust. Instead, the process is quasi-elastic, allowing us to derive an analytical solution for the surface subsidence including the volume and depth of the reservoir, the density contrast between volatiles and crust, as well as the shear modulus of the crust. This analytical solution predicts surface deformations on the order of up to a few centimeters.

We applied our scaling law to the case of the 2015 Calbuco eruption and, depending on the depth of the reservoir and volatile mass, predict subsidence of 1–4 cm, which is about 20% of the observed signal. We expect that most of the observed surface deformation is caused by the volume loss of volatiles and magma.

Adding our scaling law to existing models for volcano deformation would present a step forward, towards models that include all the relevant mechanisms that occur in volcanic roots.

Open Research Section

Software for this research is available on zenodo at:

LaMEM (Kaus et al., 2016):

http://doi.org/10.5281/zenodo.5734975

References

Annen, C., Pichavant, M., Bachmann, O., & Burgisser, A. (2008). Conditions for the growth of a long-lived shallow crustal magma chamber below Mount Pelee volcano (Martinique, Lesser Antilles Arc). *Journal of Geophysical Research: Solid Earth*, *113*(B7).

Arzilli, F., Morgavi, D., Petrelli, M., Polacci, M., Burton, M., Di Genova, D., ... Perugini, D. (2019). The unexpected explosive sub-Plinian eruption of Calbuco volcano (22–23 April 2015; Southern Chile): triggering mechanism implications. *Journal of Volcanology and Geothermal Research*, *378*, 35–50.

Bachmann, O., & Bergantz, G. W. (2004). On the origin of crystal-poor rhyolites: extracted from batholithic crystal mushes. *Journal of Petrology*, *45*(8), 1565–1582.

Blundy, J., Cashman, K. V., Rust, A., & Witham, F. (2010). A case for CO2-rich

arc magmas. *Earth and Planetary Science Letters*, *290*(3-4), 289–301.

Byerlee, J. (1978). Friction of rocks. In *Rock friction and earthquake prediction* (pp. 615–626). Birkhäuser, Basel.

Canon-Tapia, E. (2014). Volcanic eruption triggers: A hierarchical classification. *Earth-Science Reviews*, *129*, 100–119.

Castruccio, A., Clavero, J., Segura, A., Samaniego, P., Roche, O., Le Pennec, J.-L., & Droguett, B. (2016). Eruptive parameters and dynamics of the April 2015 sub-Plinian eruptions of Calbuco volcano (southern Chile). *Bulletin of Volcanology*, *78*(9), 1–19.

Crameri, F. (2018). Scientific colour-maps. *Zenodo*, *10*. doi: 10.5281/zenodo .1243862

Delgado, F., Pritchard, M. E., Ebmeier, S., González, P., & Lara, L. (2017). Recent unrest (2002–2015) imaged by space geodesy at the highest risk Chilean volcanoes: Villarrica, Llaima, and Calbuco (Southern Andes). *Journal of Volcanology and Geothermal Research*, *344*, 270–288.

Drucker, D. C., & Prager, W. (1952). Soil mechanics and plastic analysis or limit design. *Quarterly of applied mathematics*, *10*(2), 157–165.

Duretz, T., May, D. A., Gerya, T., & Tackley, P. (2011). Discretization errors and free surface stabilization in the finite difference and marker-in-cell method for applied geodynamics: A numerical study. *Geochemistry, Geophysics, Geosystems*, *12*(7).

Fialko, Y., Khazan, Y., & Simons, M. (2001a). Deformation due to a pressurized horizontal circular crack in an elastic half-space, with applications to volcano geodesy. *Geophysical Journal International*, *146*(1), 181–190.

Fialko, Y., Simons, M., & Agnew, D. (2001b). The complete (3-D) surface displacement field in the epicentral area of the 1999 mw7.1 Hector Mine earthquake, California, from space geodetic observations. *Geophysical research letters*, *28*(16), 3063–3066.

Harlow, F. H., & Welch, J. E. (1965). Numerical calculation of time-dependent viscous incompressible flow of fluid with free surface. *The physics of fluids*, *8*(12), 2182–2189.

Heap, M. J., Villeneuve, M., Albino, F., Farquharson, J. I., Brothelande, E., Amelung, F., . . . Baud, P. (2020). Towards more realistic values of elastic

moduli for volcano modelling. *Journal of volcanology and geothermal research*, *390*, 106684.

Hickey, J., Gottsmann, J., Nakamichi, H., & Iguchi, M. (2016). Thermomechanical controls on magma supply and volcanic deformation: application to Aira caldera, japan. *Scientific reports*, *6*(1), 1–10.

Hoek, E., & Brown, E. T. (1997). Practical estimates of rock mass strength. *International journal of rock mechanics and mining sciences*, *34*(8), 1165–1186.

Kaus, B. J., Mühlhaus, H., & May, D. A. (2010). A stabilization algorithm for geodynamic numerical simulations with a free surface. *Physics of the Earth and Planetary Interiors*, *181*(1-2), 12–20.

Kaus, B. J., Popov, A. A., Baumann, T., Pusok, A., Bauville, A., Fernandez, N., & Collignon, M. (2016). Forward and inverse modelling of lithospheric deformation on geological timescales. In *Proceedings of nic symposium*.

McTigue, D. (1987). Elastic stress and deformation near a finite spherical magma body: resolution of the point source paradox. *Journal of Geophysical Research: Solid Earth*, *92*(B12), 12931–12940.

Mogi, K. (1958). Relations between the eruptions of various volcanoes and the deformations of the ground surfaces around them. *Earthq Res Inst*, *36*, 99–134.

Morgado, E., Morgan, D. J., Harvey, J., Parada, M.-Á., Castruccio, A., Brahm, R., … Hammond, S. J. (2019). Localised heating and intensive magmatic conditions prior to the 22–23 April 2015 Calbuco volcano eruption (Southern Chile). *Bulletin of Volcanology*, *81*(4), 1–21.

Namur, O., Montalbano, S., Bolle, O., & Vander Auwera, J. (2020). Petrology of the April 2015 eruption of Calbuco volcano, southern Chile. *Journal of Petrology*, *61*(8), egaa084.

Newman, S., & Lowenstern, J. B. (2002). VolatileCalc: a silicate melt–H_2O–CO_2 solution model written in Visual Basic for excel. *Computers & Geosciences*, *28*(5), 597–604.

Nikkhoo, M., Walter, T. R., Lundgren, P. R., & Prats-Iraola, P. (2016). Compound dislocation models (CDMs) for volcano deformation analyses. *Geophysical Journal International*, ggw427.

Pardini, F., Burton, M., Arzilli, F., La Spina, G., & Polacci, M. (2018). SO2 emissions, plume heights and magmatic processes inferred from satellite data: The

478   2015 Calbuco eruptions.   *Journal of Volcanology and Geothermal Research*,

479   *361*, 12–24.

480 Piccolo, A., Kaus, B. J., White, R. W., Palin, R. M., & Reuber, G. S.   (2020).

481   Plume—Lid interactions during the Archean and implications for the genera-

482   tion of early continental terranes. *Gondwana Research*, *88*, 150–168.

483 Ranalli, G. (1995). *Rheology of the Earth.* Springer Science & Business Media.

484 Reuber, G. S., Kaus, B. J., Popov, A. A., & Baumann, T. S.   (2018).   Unraveling

485   the physics of the Yellowstone magmatic system using geodynamic simulations.

486   *Frontiers in Earth Science*, *6*, 117.

487 Romero, J., Morgavi, D., Arzilli, F., Daga, R., Caselli, A., Reckziegel, F., . . . Perug-

488   ini, D.   (2016).   Eruption dynamics of the 22–23 April 2015 Calbuco Volcano

489   (Southern Chile): Analyses of tephra fall deposits.   *Journal of Volcanology and*

490   *Geothermal Research*, *317*, 15–29.

491 Sigmundsson, F., Pinel, V., Grapenthin, R., Hooper, A., Halldórsson, S. A., Einars-

492   son, P., . . . Yamasaki, T.   (2020).   Unexpected large eruptions from buoyant

493   magma bodies within viscoelastic crust. *Nature communications*, *11*(1), 1–11.

494 Spang, A., Baumann, T. S., & Kaus, B. J. P.   (2021).   A Multiphysics approach

495   to constrain the dynamics of the Altiplano-Puna magmatic system.   *Journal of*

496   *Geophysical Research: Solid Earth*, *126*, e2021JB021725.

497 Spilliaert, N., Allard, P., Métrich, N., & Sobolev, A. (2006). Melt inclusion record of

498   the conditions of ascent, degassing, and extrusion of volatile-rich alkali basalt

499   during the powerful 2002 flank eruption of Mount Etna (Italy).   *Journal of*

500   *Geophysical Research: Solid Earth*, *111*(B4).

501 Turcotte, D. L., & Schubert, G. (2002). *Geodynamics.* Cambridge university press.

502 Wallace, P. J., & Gerlach, T. M.   (1994).   Magmatic vapor source for sulfur dioxide

503   released during volcanic eruptions: evidence from Mount Pinatubo.   *Science*,

504   *265*(5171), 497–499.

505 Yang, X. M., Davis, P. M., & Dieterich, J. H.   (1988).   Deformation from inflation of

506   a dipping finite prolate spheroid in an elastic half-space as a model for volcanic

507   stressing. *Journal of Geophysical Research: Solid Earth*, *93*(B5), 4249–4257.